Polymer 50 (2009) 5576–5584

Contents lists available at ScienceDirect

Polymer

journal homepage: www.elsevier.com/locate/polymer

# Microcellular and nanocellular solid-state polyetherimide (PEI) foams using sub-critical carbon dioxide I. Processing and structure

Dustin Miller, Pavee Chatchaisucha, Vipin Kumar*

*Department of Mechanical Engineering, University of Washington, Seattle, WA 98195, USA*

ARTICLE INFO

*Article history:*
Received 18 June 2009
Accepted 6 September 2009
Available online 25 September 2009

*Keywords:*
Microcellular
Nanocellular
Solid-state

ABSTRACT

In this study we investigate the solid-state batch foaming of polyetherimide (PEI) using sub-critical $CO_2$ as a blowing agent. We report on the gas diffusion for various saturation pressures in this system. Foaming process characterization is reported detailing conditions used to create microcellular and nanocellular PEI foams of 40% and higher relative density. Gas sorption, foaming, and resultant morphologies are analyzed and compared to previously reported results on PEI thin films. It was found that equilibrium gas concentrations for PEI sheet begin to significantly exceed that of films for $CO_2$ pressures above 3 MPa. A large solid-state foaming process window has been identified that allows for the creation of either microcellular or nanocellular structures at comparable density reductions. A transition from micro-scale cells to nano-scale cells was observed at gas concentrations in the range of 94–110 mg $CO_2$/g PEI. Additionally, a hierarchical structure was observed which consisted of nanocellular structures internal to microcells. The PEI–$CO_2$ system offers the unique opportunity to compare and contrast the bulk properties of nanofoams and microfoams.



## 1. Introduction

Microcellular foams refer to thermoplastic foams with cells of the order of 10 μm in size. Typically these foams are rigid, closed-cell structures. The idea to incorporate such small bubbles in thermoplastics goes back to early work at MIT t [1,2] where the advent of microcellular polystyrene was described using nitrogen as the blowing agent. The invention was in response to a challenge by food and photographic film packaging companies to reduce the amount of polymer used for packaging in their industries. Thus was born the idea to create microcellular foam, where we could have, for example, 100 bubbles across a 1 mm thickness, and expect to have a reasonable strength for the intended applications. The basic solid-state batch process used for polystyrene [1,3,4] has been used to create microcellular foams from a number of amorphous and semi-crystalline polymers, such as PVC [5], polycarbonate (PC) [6,7], acrylonitrile-butadiene-styrene (ABS) [8,9], polyethylene terephthalate (PET) [10], PETG, crystallisable polyethylene terephthalate (CPET) [11–13], and Polylactic Acid (PLA) [14–16], to name a few.

There are two basic steps in the solid-state foaming of thermoplastic polymers. The first step consists of saturation of the polymer with gas under high pressure. This step is normally carried out at room temperature. Given sufficient time for diffusion of gas into the polymer, the gas attains an equilibrium concentration that is consistent with the solubility of gas in the polymer and the gas pressure. In the second step, bubbles are nucleated in the gas–polymer system by creating a thermodynamic instability. This is achieved by either a sudden drop in pressure [17] or sudden increase in temperature [5,6]. Both strategies suddenly reduce the solubility of the gas, driving the gas out of the polymer matrix and into nucleated bubbles. One consequence of dissolving gas in the polymer is plasticization, reducing the polymer's glass transition temperature [18,19]. After saturation, the temperature of the gas-saturated polymer only needs to be raised to the glass transition temperature of the gas–polymer system to nucleate bubbles. Hence the phrase "solid-state foam" is used to describe such foams, as opposed to the conventional foams produced from a polymer melt. Microcellular foams can, however, also be produced in extrusion and injection molding during molten state [20–31].

Nanocellular foams, or nanofoams, refer to foamed polymers that have pore sizes in the range of nanometers. The idea of creating nano-scale cells in polymers is exciting but studies have been limited [3,4,9,32–42]. It has been widely hypothesized that nanofoams will offer many properties that are superior to existing materials, such as a higher strength-to-weight ratio and improved toughness. Another popular hypothesis suggests the possibility of significant improvement in thermal insulation if the cells were

* Corresponding author. Tel.: +1 (206) 543 5535; fax: +1 (206) 685 8047.
*E-mail address:* vkumar@u.washington.edu (V. Kumar).

0032-3861/$ – see front matter © 2009 Elsevier Ltd. All rights reserved.
doi:10.1016/j.polymer.2009.09.020

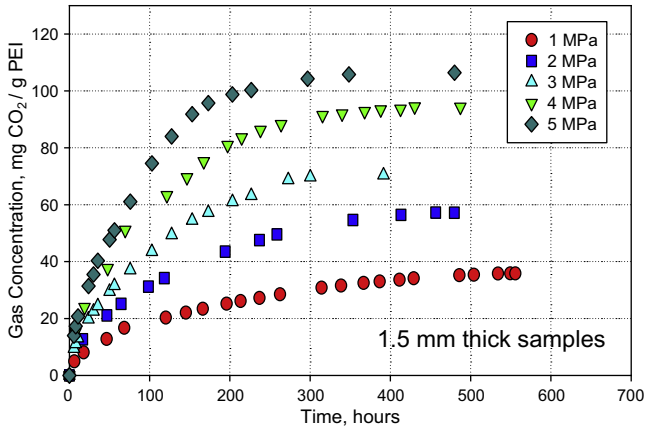


**Fig. 1.** Plots of $CO_2$ uptake as a function of time at 21 °C. Note the time needed to reach equilibrium concentration decreases as the $CO_2$ pressure increases. The data is for 1.5 mm thick specimens.

smaller than the mean free path for molecular collisions. However, thus far, no studies have been reported on mechanical or thermal properties of nanofoams.

Currently the processing techniques available to produce polymeric nanofoams are quite limited. Nanofoams have been produced for microelectronic applications using a block copolymer method [35,36], where the copolymers consist of thermally stable and thermally labile blocks. Upon heating, the thermally labile block undergoes thermolysis, leaving nanopores behind. Nanofoams with high thermal stability and relatively low dielectric constant have been produced this way. However, void fractions achieved were only in the 15–25% range. In a low-temperature process developed by Handa and Zhang [43] for PMMA–$CO_2$ system, cells in 200–400 nm range were achieved.

Microcellular foams have begun to show up in applications for automotive and food packaging industries in the last few years [44,45]. Mass-produced products envisioned from these materials include food trays, coffee cups, weather seals, and various other injection molded parts that are more environmentally friendly than current products. There is also considerable interest in the aeronautical and transportation industries to replace parts with microcellular foams taking advantage of their high strength-to-weight ratio. Additional applications include the use of microcellular plastics in liquid crystal and plasma displays as light dispersing films because of the unique properties of the small voids to disperse light evenly across the materials surface.

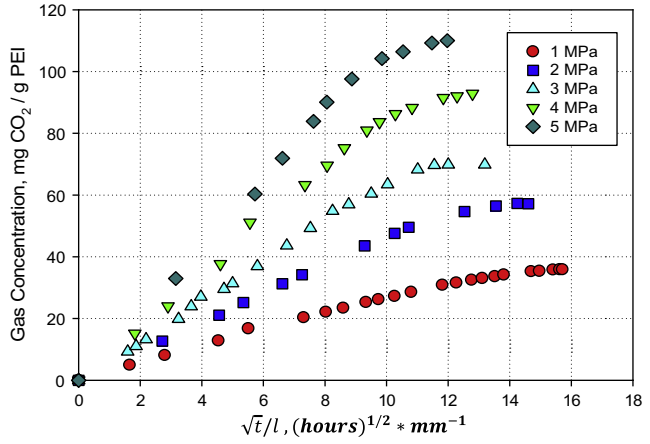


**Fig. 2.** Plots of $CO_2$ uptake as a function of time normalized for thickness at 21 °C.

**Table 1**
Time to reach equilibrium $CO_2$ concentrations for 1.5 mm thick PEI.

| Saturation pressure, MPa | Time to reach equilibrium, hours | Equilibrium concentration, mg $CO_2$/g PEI | Equilibrium concentration, $cm^3$ $CO_2$ (STP)/$cm^3$ PEI |
|---|---|---|---|
| 1 | 520 | 35.8 | 23.2 |
| 2 | 450 | 57.2 | 37.0 |
| 3 | 375 | 72.0 | 46.6 |
| 4 | 325 | 94.3 | 61.1 |
| 5 | 280 | 110.0 | 71.2 |

This study was motivated by the need for insulation and protection of electronic components at higher service temperatures. Due to its relatively high glass transition temperature, we chose to investigate PEI foams. PEI meets the stringent Federal Aviation Administration requirements for flame, smoke, and toxicity requirements as well as having a wide range of solvent resistances. We build on the work of Krause [32,33] who reported success in creating nanoporous PEI films of 75–100 μm thickness. We present an expanded set of processing conditions for the PEI–$CO_2$ system based on which bulk foams of desired thickness can be produced for different applications. As we will elaborate below, we observed significant differences in processing of sheet compared to films as well as some unique structures in PEI foams not previously reported. Most importantly, PEI–$CO_2$ system provides us, for the first time, the capability to create cellular structures at a given density where the cell size can be varied by a factor of 50–100. This capability will make it possible to investigate the effect of cell size on mechanical and other material properties of interest over a wide range of cell sizes.

## 2. Experimental

### 2.1. Materials

All of the material used in this study was Ultem 1000 PEI, made by General Electric, with a density of 1.28 g/$cm^3$, and a glass transition temperature of 215 °C. Transparent, amber colored Ultem 1000 was purchased in sheets of 1.5 mm thickness. The raw material was stored at room temperature in the original shipping packaging until sample specimens were cut for testing. The sheets were cut into 2.5 cm × 2.5 cm specimens for sorption, desorption and foaming studies.

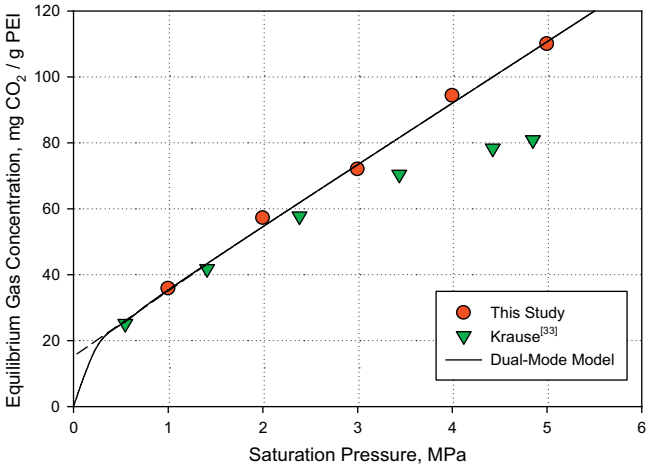


**Fig. 3.** Equilibrium gas concentration as a function of $CO_2$ saturation pressure for PEI at 21 °C. *Note: Krause data measured at 25 °C.

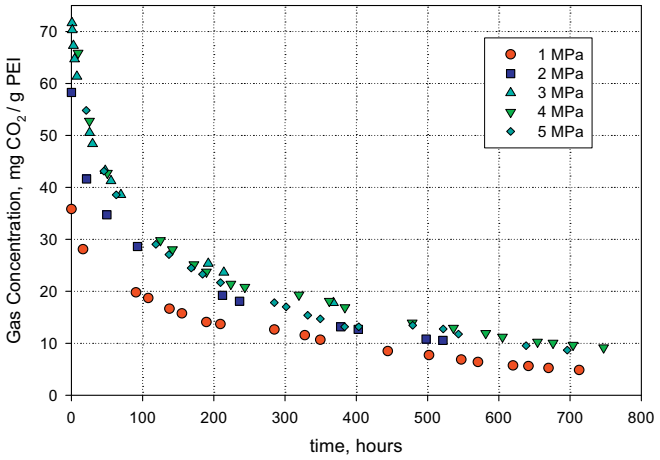


**Fig. 4.** Plots of gas concentration as a function of desorption time at 21 °C.

## 2.2. Gas saturation and desorption

The absorption and desorption of $CO_2$ in PEI was investigated. Saturation pressure, time, and temperature were controlled to vary the amount of gas delivered to the polymer. All saturation and desorption experiments were conducted at room temperature, 21 °C.

99.9% pure $CO_2$, supplied by Airgas Norpac, was delivered to the pressure vessel from a high-pressure tank. The saturation pressure was controlled by a PID microcontroller to an accuracy of +0.1 MPa. During saturation, samples were periodically removed from the pressure vessel and weighed on a METTLER AE240 balance with an accuracy of ±10 μg to measure gas uptake. Samples were then promptly returned to the pressure vessel and re-pressurized. The amount of time needed for weighing the samples was extremely small compared to the amount of time needed to achieve full saturation, so the error introduced in gas uptake measurements is not significant.

Desorption experiments of PEI samples followed a simple procedure. Samples were removed from the pressure vessel upon equilibrium saturation and allowed to desorb at room temperature and atmospheric pressure. Periodic mass measurements were taken to record the amount of gas dissolved in the sample.

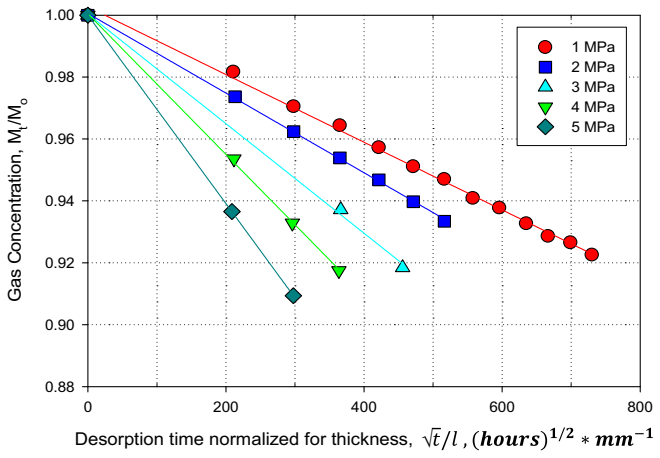


**Fig. 5.** Plots of normalized gas concentration as a function of desorption time normalized for thickness.

**Table 2**
Average diffusion coefficients calculated from initial desorption curves in Fig. 5.

| Saturation pressure, MPa | Diffusion coefficient, $cm^2/s$ |
|---|---|
| 1 | 2.33E-09 |
| 2 | 3.24E-09 |
| 3 | 6.43E-09 |
| 4 | 9.97E-09 |
| 5 | 1.80E-08 |

## 2.3. Foaming procedure

Specimens used for foaming studies were first wrapped in porous paper towel to insure that gas is absorbed by all surfaces evenly. The wrapped samples were then placed into a pressure chamber and sealed. Samples were then allowed to absorb gas over a predetermined amount of time. After samples reached full saturation they were removed from the pressure vessel and were allowed to desorb gas for 2.5 min before being foamed. A hot silicon oil bath was used to foam all of the samples used for density characterization. Following a 2 min desorption, samples were placed into the METTLER balance to measure gas concentration. At 2.5 min samples were then placed into a temperature controlled ThermoHaake B5 hot silicon oil bath and foamed for 2.5 min. Any excess oil was removed from the surface of the samples and samples were allowed to cool to room temperature in air.

## 2.4. Material characterization

The density of each sample was determined according to ASTM D792 using a Mettler AE240 analytical scale accurate to ±10 μg. Samples were allowed to desorb a minimum of 800 h before density measurements were performed in order to eliminate the effect of residual gas concentrations. After foaming a representative set of samples were imaged with a scanning electron microscope (SEM) to characterize the microstructures produced. All images were taken on a digital FEI Siriron SEM. Polymer samples were first scored with a razor blade and freeze fractured with liquid nitrogen to expose the cross sectional cellular structure. Samples were then mounted in metal stages and the imaged surface was sputter coated with Au–Pd for between 20 and 60 s. Accelerating voltages varied between 2 and 10 kV for imaging and both “high resolution” and

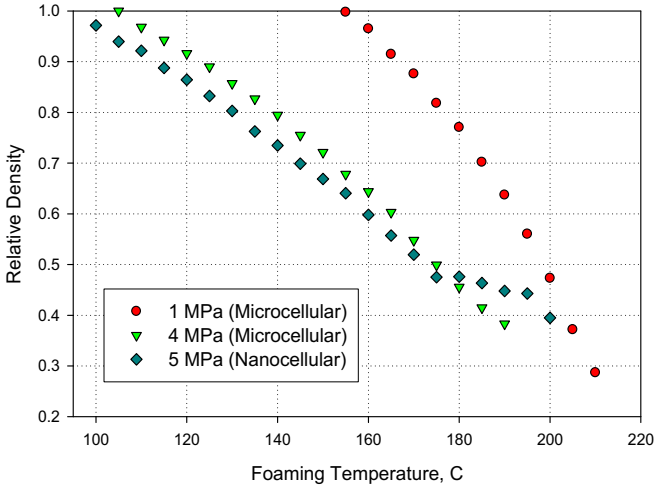


**Fig. 6.** Plot of foam relative density as a function of foaming temperature. The intersection of the data with relative density equal to 1.0 line (solid PEI) provides a good estimate for the effective glass transition temperature of the PEI–$CO_2$ system at the corresponding gas pressure.

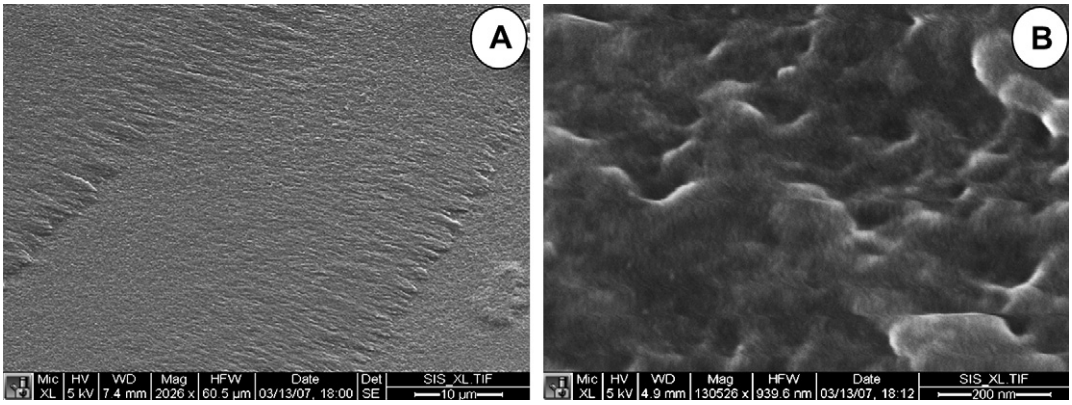


**Fig. 7.** Virgin PEI sample showing no voids. Image (A) on left at 2026× magnification and image on right (B) at 130,526× magnification.

"ultra high resolution" detectors were used depending on the size of the microstructure. Average cell size was calculated by taking average cell diameters of at least 50 cells in the SEM micrograph.

## 3. Results and discussion

We have characterized the solid-state foaming process space for PEI using sub-critical carbon dioxide and established various cellular structures produced from a wide range of processing conditions. First, the sorption and desorption behavior is established, followed by a study of foaming under various process conditions. A subset of samples from the foaming study was then analyzed to determine the range of microstructures produced. The results of the cellular structure characterization study are then related back to the processing conditions.

### 3.1. Gas sorption

Studies conducted on gas saturation and desorption reveal both essential processing requirements as well as important dynamics between the polymer and gas. Fig. 1 shows the gas uptake in units of mg $CO_2$ per g of PEI, as a function of time at various $CO_2$ pressures. We can see from Fig. 1 that the time needed to reach equilibrium concentration decreases as the $CO_2$ pressure increases. Thus, when the saturation pressure is increased from 1 MPa to 5 MPa, the time required to reach equilibrium reduces from 520 h to 280 h respectively. This is evidence of pressure-dependent diffusivity of $CO_2$ in PEI.

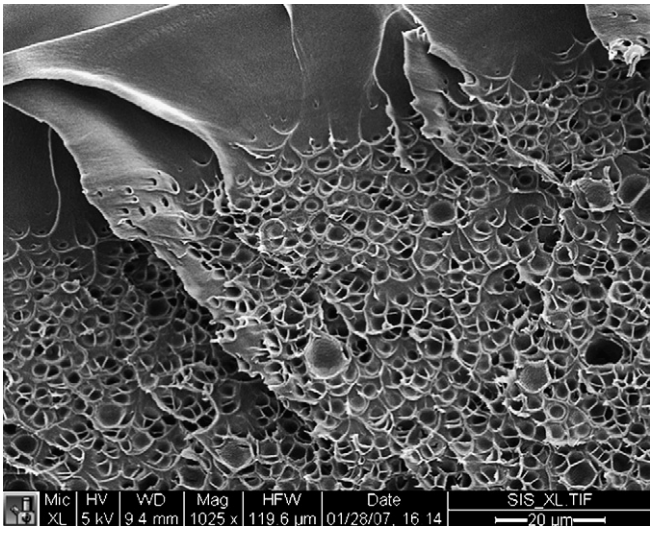


**Fig. 8.** Microcellular PEI density sample #9 showing integral skin thickness of 30 µm Horizontal bar = 20 µm (See Table 3 for processing conditions).

In Fig. 2, we have plotted the gas uptake data from Fig. 1 with the time axis normalized for thickness, in units of $(\sqrt{t}/l)$ where $t$ is time in hours, and $l$ is the specimen thickness in mm. The early part of sorption, at all pressures, shows a linear relationship between gas uptake and normalized time, indicating that diffusion follows Fick's law. Fig. 2 can be used to estimate saturation times needed for PEI sheets of different thicknesses.

The equilibrium concentrations and time required to reach equilibrium for the saturation pressures studied is summarized in Table 1. PEI presents a processing challenge due to the large times required to reach equilibrium saturation. At 1 MPa, the saturation time needed is 520 h or roughly 22 days. Long saturation times present a challenge not only to research but also to the scale-up of the solid-state process for industrial applications.

Fig. 3 shows a plot of the equilibrium $CO_2$ concentration in PEI as a function of gas pressure. Gas saturation in amorphous gas–polymer systems has been extensively studied and has been shown to be well described by the dual-mode gas sorption model in the steady state [46,47]. The dual-mode model is given by

$$C(T_{sat}, P_{sat}) = k_D(T_{sat})P_{sat} + \frac{C'_H(T_{sat})b(T_{sat})P_{sat}}{[1 + b(T_{sat})P_{sat}]} \quad (1)$$

where: $k_D(T_{sat})$ is Henry's gas law constant, $C'_H(T_{sat})$ is the capacity constant for Langmuir mode adsorption, $b(T_{sat})$ is the affinity constant of the Langmuir mode sites, $P_{sat}$ is the applied gas saturation pressure, and $T_{sat}$ is the saturation temperature. The Dual-mode sorption model requires that the relationship between saturation pressure and equilibrium concentration be linear for a high saturation pressures and that the zero pressure intercept of this relationship be given by the Langmuir capacity constant.

The equilibrium concentration and saturation pressure relationship is linear for PEI sheet in this study above 1 MPa, following Henry's law:

$$C(T_{sat}, P_{sat}) = k_D(T_{sat}) \times P_{sat} \quad (2)$$

In Eq. (2), $C$ is the equilibrium gas concentration, $P_{sat}$ is the gas saturation pressure, and $k_D$ is the Henry's Law constant, estimated to be 18.55 mg $CO_2$/g PEI/MPa, or 1.20 $cm^3$ $CO_2$ STP/$cm^3$ PEI/bar for the PEI–$CO_2$ system. In previous studies of $CO_2$ sorption in PETG, PC and PVC [6,12,48] the equilibrium gas concentration also obeyed the Henry's Law for high pressures in the sub-critical range. The Langmuir mode adsorption constant is estimated from the intercept of the extrapolated high-pressure gas sorption isotherm. From

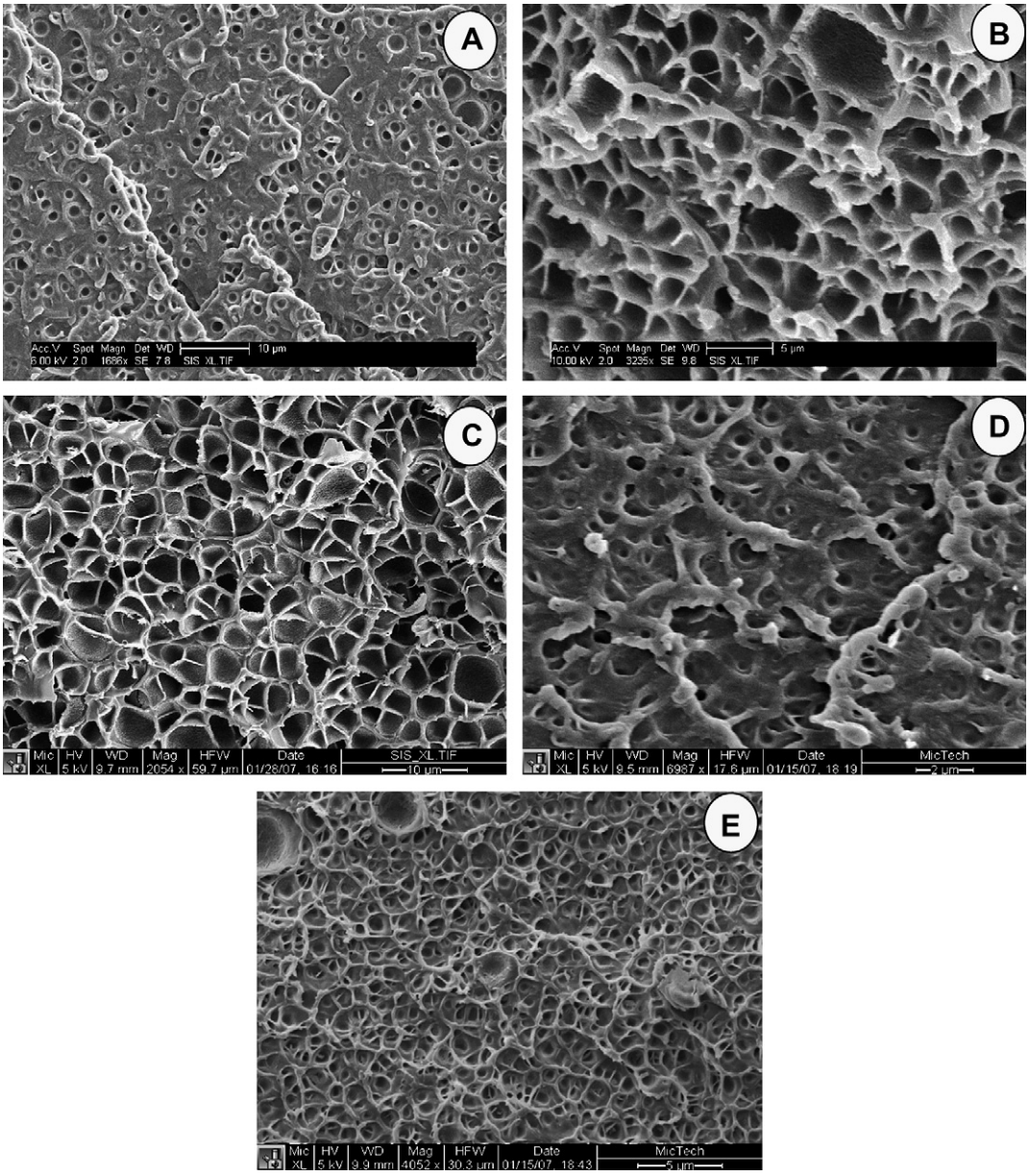


**Fig. 9.** Microcellular PEI structures created at 1 MPa (A–C) and 4 MPa (D,E) saturation pressures. (A) Sample #3 bar = 10 μm, (B) Sample #7 bar = 5 μm, (C) Sample #9 bar = 10 μm, (D) Sample #18 bar = 2 μm, (E) Sample #24 bar = 5 μm. Sample numbers correspond to Table 3.

Fig. 3 the Langmuir mode adsorption ($C'_H$) is estimated to be 18.21 mg $CO_2$/g PEI or 11.82 $cm^3$ $CO_2$ STP/$cm^3$ PEI. The Langmuir hole affinity (b) is estimated by fitting low saturation pressure sorption isotherm curvature and is estimated from Fig. 3 to be 12 $MPa^{-1}$ or 1.2 $bar^{-1}$.

In Fig. 3 we also compare sorption data in this study to that reported by Krause [33], which was taken on 75–100 μm thick PEI films. We see that the data agrees up to about 3 MPa saturation pressure. At higher pressures the equilibrium absorption in bulk PEI is significantly higher than that achieved in film; nearly 40% higher at 5 MPa. The referenced data for PEI thin films does not follow Henry's Law and thus the linear range for the dual-mode sorption model for high saturation pressures. Variations in gas concentrations between thin films and sheet material may cause significant differences in the solid-state foam microstructures produced.

Equally important to gas saturation in the solid-state process is desorption of gas when the gas pressure is released from the pressure vessel. Typically, desorption times are limited to small time periods during foaming to prevent significant amounts of gas from escaping from the polymer. However, desorption data also reveals important characteristics of the gas diffusion kinetics. Data collected on desorption of the fully saturated PEI samples is shown in Fig. 4 for various saturation pressures. Even after long desorption periods, solid saturated PEI samples still have significant amounts of gas dissolved. In order to minimize error in density measurements due to dissolved gas, foamed samples were desorbed a minimum of 800 h (33.3 days) before density measurements were taken.

The initial desorption data points from Fig. 4 are shown in Fig. 5, normalized both for sample thickness and gas concentration. In Fig. 5, $M_o$ is the mass of $CO_2$ dissolved in the specimen at equilibrium, and $M_t$ is the mass of $CO_2$ remaining in the specimen after desorbing for $t$ h. From Fig. 5 we calculate the average diffusion coefficients for the various concentrations following the procedure proposed by Crank [49]. Diffusion coefficients are summarized in Table 2 and show that PEI has concentration dependant diffusion at these concentrations.

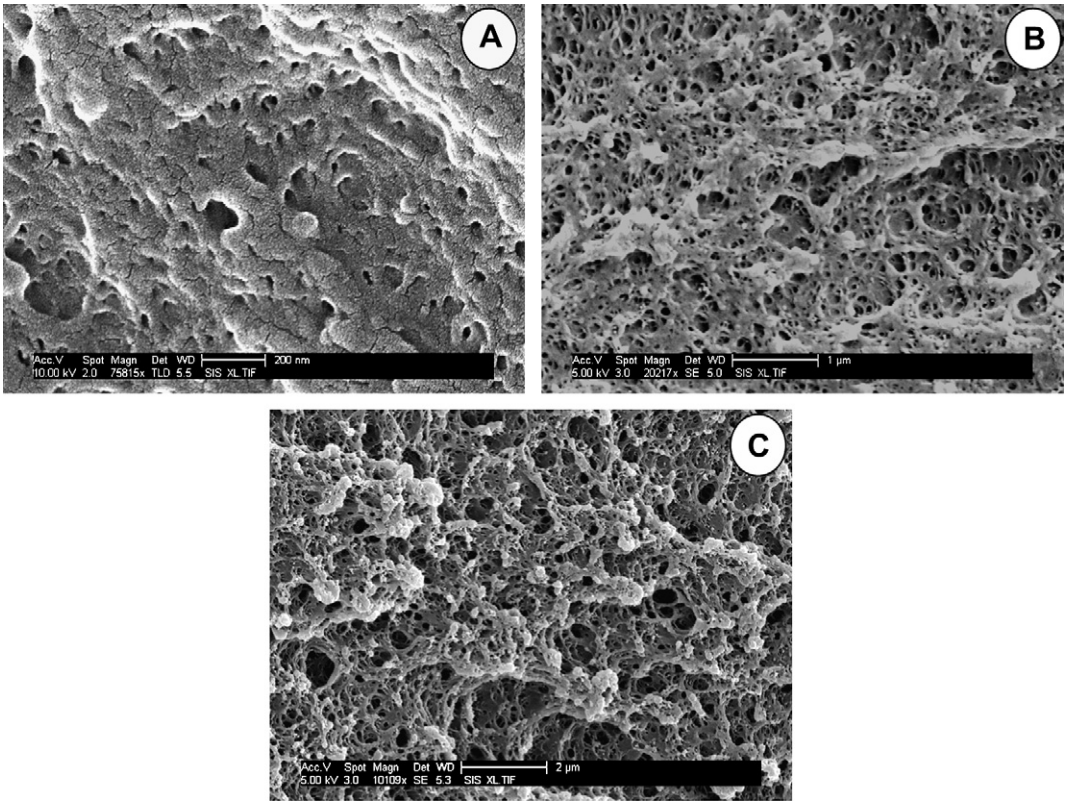


**Fig. 10.** Nanocellular PEI structures created at 5 MPa saturation pressure. (A) Sample #40 bar = 200 nm, (B) Sample #43 bar = 1 µm, (C) Sample #47 bar = 2 µm.

### 3.2. Solid-state foaming and cellular structure

Fig. 6 shows the foam relative density (density of foam/PEI density) as a function of foaming temperature for saturation pressures of 1, 4 and 5 MPa. From prior work there exists a micro to nano cell size transition point between 4 and 5 MPa [33]. 1 and 5 MPa saturation pressure solid-state foaming characterization experiments were performed to map the processing space of micro- and nanocellular PEI. The experiments consisted of saturating samples of PEI and foaming within a wide range of temperature conditions. The relative densities of the foamed samples were then measured after long desorption periods to reduce the influence of residual gas concentrations.

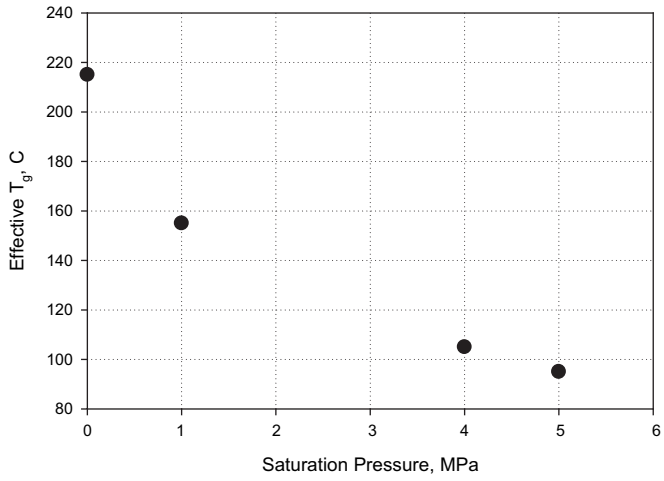


**Fig. 11.** Glass transition temperature as a function of saturation pressure estimated from data in Fig. 6. Note the significant reduction in $T_g$ at 4 and 5 MPa $CO_2$ pressures.

The 4 MPa characterization experiment was performed to see if the resulting structure was nanocellular, or a combination of micro and nano cells. Samples were saturated at 4 MPa to full saturation based upon saturation experiments and then were foamed at various temperatures to study structure and density. Samples were evaluated to see how saturation pressure and foaming temperature affected the structure of the PEI foam produced. In Fig. 6 we see that as foaming temperature is increased, density of the foam produced decreases orderly over a large temperature range.

Representative samples from the solid-state foaming process space study were imaged by SEM to characterize the structures resulting from the various processing conditions. The primary motivation of this work was to explore the various microstructures that could be produced at like densities. Analysis of the foam morphology consisted of quality characteristics such as average cell size, cell density and skin thickness. Before images were taken of the foam structure, solid PEI was first imaged to determine if the neat material exhibited any porosity at the micro or nano level. Fig. 7 are images of solid PEI at two different scales. As can been seen from these images, no porosity exists at either the micro or nano scale.

Skin thickness measurements were done on samples imaged and the results from the image analysis reveal that skin thickness was independent of the scale of cellular structure. Fig. 8 shows the skin thickness of a typical microcellular PEI sample. Skin thickness was found to depend upon desorption time before foaming and the final sample density. These results for skin thickness are consistent with previous studies [50].

SEM micrographs reveal the vast differences between samples saturated at 1 and 5 MPa. Fig. 9 shows the microcellular structures produced at 1 and 4 MPa and Fig. 10 is a collection of nanocellular structures produced at 5 MPa with roughly the same density ranges

**Table 3**
Processing conditions and results.[a]

| Sample # | Saturation pressure (MPa) | Foaming temperature (C) | Relative density | Avg. cell size | Cell density (cells/cm$^3$) | Comments (Figure #) |
|---|---|---|---|---|---|---|
| 1 | 1 | 155 | 99.8% | | | |
| 2 | 1 | 160 | 96.5% | | | |
| 3 | 1 | 165 | 91.5% | 2 μm | $3.8\times10^{10}$ | 9A |
| 4 | 1 | 170 | 87.6% | | | |
| 5 | 1 | 175 | 81.8% | | | |
| 6 | 1 | 180 | 77.0% | 2 μm | $4.28\times10^{10}$ | |
| 7 | 1 | 185 | 70.2% | 3 μm | $5.1\times10^{10}$ | 9B |
| 8 | 1 | 190 | 63.7% | | | |
| 9 | 1 | 195 | 56.0% | 4 μm[a] | $8.5\times10^{10}$ | 8, 9C, 12 |
| 10 | 1 | 200 | 47.3% | 4 μm[a] | $12.9\times10^{10}$ | |
| 11 | 1 | 205 | 37.2% | | | |
| 12 | 1 | 210 | 28.7% | | | |
| 13 | 4 | 105 | 100.0% | | | |
| 14 | 4 | 110 | 96.8% | | | |
| 15 | 4 | 115 | 94.2% | | | |
| 16 | 4 | 120 | 91.6% | | | |
| 17 | 4 | 125 | 89.0% | | | |
| 18 | 4 | 130 | 85.7% | 1 μm | $3.85\times10^{10}$ | 9D |
| 19 | 4 | 135 | 82.7% | | | |
| 20 | 4 | 140 | 79.5% | | | |
| 21 | 4 | 145 | 75.5% | | | |
| 22 | 4 | 150 | 72.1% | | | |
| 23 | 4 | 155 | 67.8% | | | |
| 24 | 4 | 160 | 64.4% | 1 μm | $7.8\times10^{10}$ | 9E |
| 25 | 4 | 165 | 60.3% | | | |
| 26 | 4 | 170 | 54.8% | | | |
| 27 | 4 | 175 | 49.9% | | | |
| 28 | 4 | 180 | 45.5% | | | |
| 29 | 4 | 185 | 41.5% | | | |
| 30 | 4 | 190 | 38.3% | | | |
| 31 | 5 | 100 | 97.1% | | | |
| 32 | 5 | 105 | 94.0% | | | |
| 33 | 5 | 110 | 92.2% | | | |
| 34 | 5 | 115 | 88.8% | | | |
| 35 | 5 | 120 | 86.4% | | | |
| 36 | 5 | 125 | 83.2% | | | |
| 37 | 5 | 130 | 80.3% | | | |
| 38 | 5 | 135 | 76.2% | | | |
| 39 | 5 | 140 | 73.5% | | | |
| 40 | 5 | 145 | 69.9% | 30 nm | $2.00\times10^{14}$ | 10A |
| 41 | 5 | 150 | 66.9% | | | |
| 42 | 5 | 155 | 64.0% | | | |
| 43 | 5 | 160 | 59.8% | 50 nm | $2.13\times10^{14}$ | 10B |
| 44 | 5 | 165 | 55.7% | | | |
| 45 | 5 | 170 | 51.9% | 80 nm | $2.00\times10^{14}$ | |
| 46 | 5 | 175 | 47.5% | | | |
| 47 | 5 | 180 | 47.6% | 120 nm | $1.36\times10^{14}$ | 10C |
| 48 | 5 | 185 | 46.3% | | | |
| 49 | 5 | 190 | 44.8% | | | |
| 50 | 5 | 195 | 44.3% | | | |
| 51 | 5 | 200 | 39.5% | | | |

[a] Samples showing nanostructure internal to microcells as is displayed in Fig. 12.

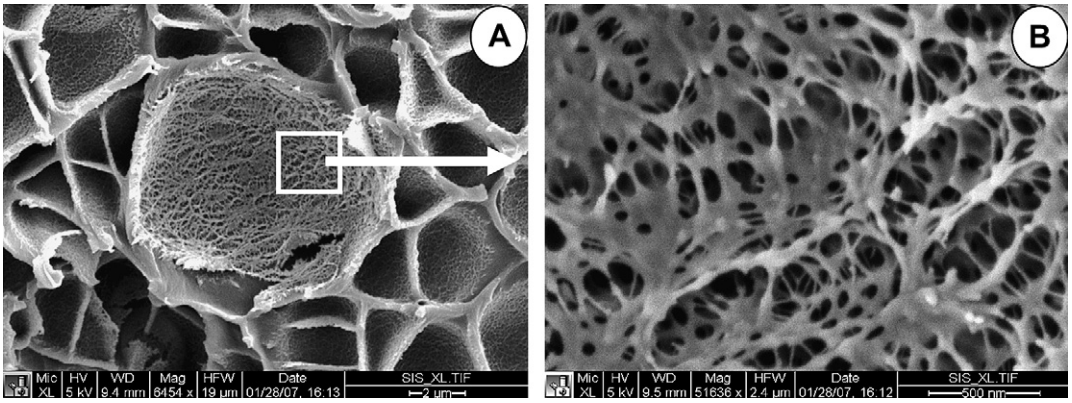


**Fig. 12.** Microcellular sample #9, 56.0% relative density, showing nano features on internal cell wall. (A) bar = 2 μm, (B) focus area of interior of cell wall shown in (A), (B) bar = 500 nm.

as that of the microcellular samples. Microcellular PEI samples exhibit average cell sizes in the range of 1–5 μm and cell densities on the order of $10^{10}$ cells/cm$^3$. Nanocellular samples produced have average cell sizes ranging from 30 to 120 nm and cell densities on the order of $10^{14}$ cells/cm$^3$. Between the saturation pressure of 4 and 5 MPa, the cell size drops from around 1 μm to 70 nm and cell densities increase from $10^{10}$ to $10^{14}$ cells/cm$^3$.

The variation in cell sizes and nucleation densities between 4 and 5 MPa were also found by Krause [33]. Although there are similarities between the saturation pressures, we have found that equilibrium gas concentrations vary between thin films and sheet (Fig. 3). Krause found that the micro/nano transition region occurred between 47 and 49 cm$^3$ $CO_2$/cm$^3$ PEI or 72–75 mg $CO_2$/g PEI for thin films verified by both SEM and gas permeation measurements. This study reveals that the micro/nano transition for sheet lies between 94 and 110 mg $CO_2$/g PEI.

The average cell sizes of the microcellular and nanocellular samples vary in magnitude by 100×. The foam structure of nanocellular PEI holds much promise for future material characterization due to the size of its structures. Average cell sizes have now entered into the nanometer dimensional range where the bubbles are on the same order as that of the polymer's molecular chains. Also, cell sizes observed are smaller than the mean free path of air at atmospheric temperature and pressure. Limiting this mean free path to less than ambient conditions may cause a breakdown in the conductive heat transport through the gas bubbles of the foam. It is because of these two facts that many have hypothesized that these nanocellular polymers will exhibit unique mechanical and thermal properties to that of conventional and microcellular foams. Now that detailed processing conditions have been presented, future studies can attempt to answer some of these questions.

The horizontal lines of the foaming plot in Fig. 6 shows that PEI foams with a given density can be produced at different saturation pressures above 40% relative density. The well defined relative density foaming temperature plot allows for an accurate model to produce specific densities above 40% relative density for future testing. At foaming temperatures above 200 °C the samples saturated at 5 MPa began to have a more erratic behavior during foaming. Such cracking and erratic foaming behavior was also seen in 4 MPa saturated specimens at foaming temperatures above 200 °C. Typically in the solid-state process foaming temperatures can approach the glass transition temperature of the neat polymer, as is the case for the 1 MPa saturated PEI samples capable of density reductions up to PEI's glass transition temperature of 215 °C. It is unclear why both 4 and 5 MPa saturated samples exhibited cracking and uneven foaming before this temperature point.

Another interesting insight from Fig. 6 is the minimum foaming temperatures that first result in observed nucleation and density reduction shown by where the foaming data intersects with a relative density of 1.0. From the plot we see that the minimum foaming temperature values are well below the reported glass transition temperature of the neat polymer due to the suppression of the glass transition temperature by the presence of $CO_2$. The effective glass transition temperature defines the transition temperature of a gas–polymer mixture at which the polymer molecular chains exhibit mobility and chain sliding. The addition of gas molecules to a polymer system decreases the effective glass transition temperature and thus increases polymer mobility. This mechanism is one of the primary driving mechanisms in the solid-state foaming of microcellular plastics.

The minimum foaming temperature and the effective glass transition temperature of the gas–polymer system can be considered to be equivalent [51]. Thus, the minimum foaming temperature for a given gas pressure provides a good estimate of the effective glass transition temperature of the gas–polymer system. Fig. 11 below shows the effective $T_g$ values estimated from the relative density plot in Fig. 6. This data shows that the dissolved $CO_2$ reduces the $T_g$ of PEI significantly. At 5 MPa, for example, the $T_g$ reduces from 215 °C for virgin PEI to 95 °C, a change of 120 °C. This reduction in $T_g$ can offer advantages in processing PEI, such as lower energy input and/or reduction in process temperatures.

In Table 3 we summarize the results from the foaming experiments. The density produced at each processing condition is listed. Also included in the table is data on cell size and nucleation density collected from selected specimens. Table 3 can also be used to cross reference micrograph images with processing conditions and cellular structure analysis. From this table we can observe the processing conditions and resultant cell sizes and foam cell density. Saturation pressures of 1 and 4 MPa result in cell densities ranging from 3.8 to $12.9 \times 10^{10}$ cells per cubic centimeter. These two saturation pressures also show overlap in cell density where cell density is highly a function of foaming temperature. In contrast, 5 MPa saturation pressure increases cell density by 10,000×. Along with cell density, cell size reduces from 2 to 4 μm for saturation pressures between 1 and 4 MPa to between 30 and 120 nm for a saturation pressure of 5 MPa. Density, which is a function of cell size and number of cells (cell density), ranges from 30 to 99% of that of the solid. The result of this comparison is that two very different cellular structures can be produced in the same polymer at the same given density.

A unique structure was observed while imaging the microstructures created at 1 MPa. This unique structure was found in microcellular samples where the density of the sample was less than 60% relative to the solid. Images of lower relative density microcellular samples are shown in Fig. 12A&B. These samples exhibit the normal microcellular structure, but upon closer inspection, the inner cell walls show many nano-sized features. The micrograph images appear to show that the microcellular walls are composed of a nanocellular structure. Fig. 12 B is the nano-sized structure that resides on the internal cell wall of the primary microcellular structure. This nano-sized structure appears to be openly porous at least for small distances into the microcellular wall. The size of the cells in the internal structure appears to be around 100 nm with cellular struts less than 60 nm.

The structure of having cells within cells will from now on be termed as a "hierarchical structure". The hierarchical structure is unique compared to all other solid-state foaming structures observed in published microcellular research. The main question regarding this hierarchical structure is; how is this structure made? All proposed mechanisms for this phenomenon are just conjecture at this point since no further experimentation was conducted. For lower density samples, it appears that a subsequent stage of cell nucleation and growth is occurring after that of the initial nucleation during the foaming stage. This secondary nucleation could be a product of stress-induced nucleation or spinodal decomposition. Spinodal decomposition is the separation of two or more components into distinct regions occurring uniformly throughout the material rather than classical nucleation of discrete nucleation sites. The open structure observed in Fig. 12 B displays this uniform continuous phase separation.

In addition to these nano features, samples with lower densities appear to have interconnectivity approximately when the cells begin to share cell walls with neighboring cells. There exist many methods to determine interconnectivity including die diffusion and gas permeability testing. None of these methods were utilized in this research, but provide opportunity for future work.

## 4. Summary

The solid-state batch process using subcritical $CO_2$ offers a unique process by which large variations in cellular structure size can be produced in PEI sheet. This research presents a processing range where cellular PEI foams can be created at like densities

between 40 and 99% relative densities to that of the solid and cellular structures vary by a factor of 100×. The PEI foams produced present an opportunity to achieve high temperature foams that can be tailored to specific densities and thus material property requirements.

Sorption plots, Figs. 1–5, show that equilibrium concentrations of $CO_2$ are a function of saturation pressure and sorption rate of $CO_2$ in PEI is concentration dependent. Comparing PEI sheet (1.5 mm thick) saturation to that of previous work by Krause [33] on thin films, it was found that above saturation pressures of 3 MPa, the equilibrium gas concentration of $CO_2$ in sheet continues to increase linearly with saturation pressure, obeying Henry's Law unlike that found for PEI film. PEI sheet absorbs almost 40% more gas by weight at 5 MPa when compared to PEI film.

Solid-state foaming of PEI sheet for various saturation pressures is presented in Fig. 6. The results from this foaming study reveal a large density range that can be produced. Also from this plot we see that PEI exhibits a significant drop in the polymers glass transition temperature due to dissolved $CO_2$. At 5 MPa $CO_2$ pressure, the glass transition temperature is lowered to 95 °C from 215 °C of the neat polymer. This reduction in the glass transition temperature can offer advantages in processing PEI, such as lower energy input and/or reduction in process temperatures.

Microscopy of the PEI samples produced display a considerable contrast in foam morphology between samples produced at 1 and 5 MPa. 1 MPa saturated microcellular samples have cell sizes between 2 and 4 μm with cell densities on the order of $10^{10}$ cells/$cm^3$. When the saturation pressure is raised to 5 MPa, nanocellular structures are produced with cell sizes between 30 and 120 nm and cell densities on the order of $10^{14}$ cells/$cm^3$. A transition from micro scale cells to nano-scale cells was observed at gas concentrations in the range of 94–110 mg $CO_2$/g PEI. A third cellular structure was also observed when samples are saturated at 1 MPa and foamed to densities below approximately 60% relative density. This hierarchical structure shown in Fig. 12 has a primary microcellular structure with 4 μm sized cells. The internal cell wall is composed of a nanocellular foam structure with cells on the order of 60–100 nm. This hierarchical structure may be due to spinodal decomposition in the microcell walls.

The results of this study enable the creation of high temperature PEI foams and the tailoring of foam density for application. In order to bring these materials to market, future material testing studies are needed to determine the properties of these foams. Although the mechanisms that create such a large cell size difference in PEI are still not understood, microcellular and nanocellular foams can now be created in a bulk form to determine if nanocellular foams will offer unique advantageous properties. This new result now allows for a unique opportunity to compare and contrast the material properties of nanocellular and microcellular foams independent of material and density. Many researchers in the microcellular foams community have hypothesized that nanocellular foams will offer greater benefits in mechanical and thermal properties over conventional and microcellular foams, but until now, these hypotheses have been difficult to impossible to test. The data presented in Fig. 6 now presents a clear path to test these hypotheses by presenting the processing conditions needed to create material testing samples.

## References


[1] Martini J, Suh NP, Waldman FA. Microcellular closed cell foams and their method of manufacture. Pat. #4473665. USA: Massachusetts Institute of Technology; 1984.
[2] Martini J, Waldman FA, and Suh NP. The production and analysis of microcellular thermoplastic foam. SPE ANTEC: vol. 28. San Francisco, CA; 1982. p. 674.
[3] Otsuka T, Taki K, Ohshima M. Macromolecular Materials and Engineering 2008;293(1):78–82.
[4] Taki K, Waratani Y, Ohshima M. Macromolecular Materials and Engineering 2008;293(7):589–97.
[5] Kumar V, Weller JE. International Polymer Processing 1993;VIII(I):73–80.
[6] Kumar V, Weller JE. Journal of Engineering in Industry 1994;116:413–20.
[7] Collias DI, Baird DG, Borggreve RJM. Polymer 1994;35:3978–83.
[8] Murray RE, Weller J, Kumar V. Cellular Polymers 2000;19(6):413–25.
[9] Nawaby V, Handa P. Fundamental Understanding of the ABS–$CO_2$ interactions, its retrograde behavior and development of nanocellular structures. ANTEC: vol. 2. Chicago, IL; 2004. p. 2532–6.
[10] Shimbo M, Higashitani I, Miyano Y. Journal of Cellular Plastics 2007;43:157–67.
[11] Kumar V, Gebizlioglu OS. SPE Technical Papers 1992;38:1536–40.
[12] Handa YP, Wong B, Zhang Z, Kumar V, Eddy S, Khemani K. Polymer Engineering and Science 1999;39(1):55–9.
[13] Kumar V, Juntunen RP, Barlow C. Cellular Polymers 2000;19(1):25–37.
[14] Kumar V, Li W, Wang X. A Study of PLA crystallization during solid-state foaming. In: NSF engineering research innovation conference. Knoxville, Tennessee; 2008.
[15] Richards E, Rizvi R, Chow A, Naguib H. Journal of Polymers and the Environment 2008;16:258–66.
[16] Wang X, Kumar V, Li W. Cellular Polymers Jan 2007;26(1).
[17] Goel SK, Beckman EJ. Cellular Polymers 1993;12(4):251.
[18] Chow TS. Macromolecules 1980;13:362–4.
[19] Zhang Z, Handa YP. Journal of Polymer Science 1998;36:977–82.
[20] Baldwin DF, Park CB, Suh NP. Polymer Engineering & Science 1996;36(10):1425–35.
[21] Behravesh AH, Park CB, Venter RD. Approach to the production of low-density, microcellular foams in extrusion. In: SPE ANTEC. Atlanta; 1998. p. 1958–67.
[22] Han X, Koelling KW, Tomasko DL, Lee LJ. Polymer Engineering & Science 2002;42(11):2094–106.
[23] Han X, Zeng C, Lee LJ, Koelling KW, Tomasko DL. Polymer Engineering & Science 2003;43(6):1261–75.
[24] Klotzer R, Paul D, Seibig B. Extrusion of microcellular foams and application. In: SPE ANTEC. Toronto; 1997. p. 2042–5.
[25] Kumar V, Nadella K, Branch G, Flinn B. Cellular Polymers 2004;23(6):369–85.
[26] Park CB, Behravesh AH, Venter RD. Polymer Engineering & Science 1998;38(11):1812–23.
[27] Park CB, Suh NP. Polymer Engineering & Science 1996;36(1):34–48.
[28] Park CB, Suh NP. Extrusion of microcellular polymers using a rapid pressure drop device. In: SPE ANTEC. New Orleans; 1993. p. 1818–21.
[29] Schirmer HG, Kumar V. Cellular Polymers 2003;22(3):157–74.
[30] Shimbo M, Nishida K, Nishikawa S, Sueda T, Eriguti M. Porous, Cellular and Microcellular Materials: ASME 1998;82:93–8.
[31] Xanthos M, Yilmazer U, Dey SK, Quintans J. Polymer Engineering & Science 2000;40(3):554–66.
[32] Krause B, Diekmann K, Van Der Vegt NFA, Wessling M. Macromolecules 2002;35:1738–45.
[33] Krause B, Sijbesma HJP, Munuklu P, Van Der Vegt NFA, Wessling M. Macromolecules 2001;34:8792–801.
[34] Chatchaisucha P, Kumar V. Micro and nano scale solid-state PEI foams. In: SPE ANTEC. Charlotte, NC; 2006.
[35] Hedrick JL, Carter KR, Cha HJ, Hawker CJ, DiPietro RA, Labadie JW, et al. Reactive and Functional Polymers 1996;30:43–53.
[36] McGrath JE, Jayaraman SK, Lakshmanan P, Abed JC, Afchar-Taromi F. Polyimide nanofoams: Materials design and development. In: Proceedings of the ACS New Orleans Meeting. New Orleans; 1996. p. 136–7.
[37] Miller D, Kumar V. Micro and Nanocellular HDPE Foams. In: SPE Foams. Charlotte, NC; 2008.
[38] Nawaby V, Handa P, Liao X, Yoshitaka Y, Tomohiro M. Polymer International 2007;56:67–73.
[39] Nemoto T, Takagi J, Ohshima M. Macromolecular Materials and Engineering 2008;293(7):574–80.
[40] Nemoto T, Takagi J, Ohshima M. Macromolecular Materials and Engineering 2008;293(12):991–8.
[41] Siripurapu S, Coughlan J, Spontak R, Khan S. Macromolecules 2004;37:9872–9.
[42] Baldwin DF, Suh NP, Park CB, Cha SW. Supermicrocellular foamed materials. Pat. #5,334,356. USA: Massachusetts Institute of Technology; 1994.
[43] Handa YP, Zhang Z. Manufacturing ultramicrocellular polymer foams at low pressure. Pat. #5,955,511. USA; 1999.
[44] Trexel MuCell Processes. Trexel, Inc; 2006.
[45] MicroGREEN Polymers. Advanced plastics for everyday living. MicroGREEN Polymers, Inc.; 2005.
[46] Koros WJ, Paul DR, Rocha AA. Journal of Polymer Science: Polymer Physics Edition 1976;14(4):687–702.
[47] Kamiya Y, Hirose T, Mizoguchi K, Naito Y. Journal of Polymer Science, Part B: Polymer Physics 1986;24:1525–39.
[48] Juntunen RP, Kumar V, Weller J, Bezubic WP. Journal of Vinyl and Additive Technology 2000;6(2):93–9.
[49] Crank J. In: The mathematics of diffusion. 2nd ed. New York: Oxford Science Press; 1989.
[50] Kumar V, Weller J. Polymer Engineering and Science 1994;34(3):169–73.
[51] Kumar V, Weller JE, Montecillo R. ANTEC; 1992. p. 1452–6.